Soft Matter

PAPER

View Article Online
View Journal | View Issue

Cite this: *Soft Matter*, 2016, 12, 7782

Influence of surfactants in forced dynamic dewetting†

Franziska Henrich, Daniela Fell, Dorota Truszkowska, Marcel Weirich, Manos Anyfantakis, Thi-Huong Nguyen, Manfred Wagner, Günter K. Auernhammer* and Hans-Jürgen Butt

Received 28th April 2016,
Accepted 19th August 2016

DOI: 10.1039/c6sm00997b

www.rsc.org/softmatter

In this work we show that the forced dynamic dewetting of surfactant solutions depends sensitively on the surfactant concentration. To measure this effect, a hydrophobic rotating cylinder was horizontally half immersed in aqueous surfactant solutions. Dynamic contact angles were measured optically by extrapolating the contour of the meniscus to the contact line. Anionic (sodium 1-decanesulfonate, S-1DeS), cationic (cetyl trimethylammonium bromide, CTAB) and nonionic surfactants (C_4E_1, C_8E_3 and $C_{12}E_5$) with critical micelle concentrations (CMCs) spanning four orders of magnitude were used. The receding contact angle in water decreased with increasing velocity. This decrease was strongly enhanced when adding surfactant, even at surfactant concentrations of 10% of the critical micelle concentration. Plots of the receding contact angle-*versus*-velocity almost superimpose when being plotted at the same relative concentration (concentration/CMC). Thus the rescaled concentration is the dominating property for dynamic dewetting. The charge of the surfactants did not play a role, thus excluding electrostatic effects. The change in contact angle can be interpreted by local surface tension gradients, *i.e.* Marangoni stresses, close to the three-phase contact line. The decrease of dynamic contact angles with velocity follows two regimes. Despite the existence of Marangoni stresses close to the contact line, for a dewetting velocity above 1–10 mm s^{-1} the hydrodynamic theory is able to describe the experimental results for all surfactant concentrations. At slower velocities an additional steep decrease of the contact angle with velocity was observed. Particle tracking velocimetry showed that the flow profiles do not differ with and without surfactant on a scales >100 μm.

Introduction

The wetting and dewetting of a solid surface by a liquid are fundamental processes of many natural phenomena and technical applications. Examples are the movement of a drop running down a window glass or being blown across a windscreen, coating, painting, printing, and the distribution of pesticides on leaf surfaces. Wetting is characterized by the contact angle formed at the three-phase contact line. In equilibrium, the contact angle (Θ) on an ideally smooth, homogeneous and nondeformable surface is determined by a balance of the interfacial tensions:[1]

$$\cos\Theta_e = \frac{\gamma_S - \gamma_{SL}}{\gamma_L} \quad (1)$$

Here, γ_S, γ_{SL} and γ_L are the interfacial tensions of the solid–air, the solid–liquid, and the liquid–air interfaces, respectively. In practice, when placing a drop on a real surface a drop can assume a range of static contact angles. This range is limited by an upper value, the advancing contact angle, and a lower value, the receding contact angle. The difference between the two is called contact angle hysteresis. Even on the most homogeneous and cleanest surfaces finite contact angle hysteresis is observed.

When the contact angle exceeds the range between the advancing and receding contact angle, the contact line starts moving. In this case the contact angle depends on the velocity and one observes dynamic contact angles. Such a situation can arise when *e.g.* a drop is placed on a surface and its initial contact angle is significantly larger than the advancing contact angle. It spontaneously spreads driven by interfacial, also called capillary forces. Movement of the contact line can also be caused by external forces such as gravity. In contrast to spontaneous wetting/dewetting, in which a liquid is drawn towards its equilibrium configuration by capillary forces, in forced wetting/dewetting external forces continuously maintain a certain velocity of the contact line. One of the key questions in wetting dynamics is: how are velocity and dynamic contact angle related?

Here, we focus on forced dewetting that is, for example, essential in coating. Several techniques have been employed to measure dynamic receding contact angles. In early experiments,

Max Planck Institute for Polymer Research, Ackermannweg 10, 55128 Mainz, Germany. E-mail: auhammer@mpip-mainz.mpg.de

† Electronic supplementary information (ESI) available. See DOI: 10.1039/c6sm00997b

thin capillaries have been used to measure dynamic contact angles over a range of velocities.[2,3] When plotting the dynamic contact angles *versus* the capillary number rather than velocity U, all results collapsed onto a single master curve.[3] The capillary number $\mathrm{Ca} = \eta U/\gamma_L$ represents the relative effect of viscous forces *versus* the surface tension; η is the viscosity of the liquid. A disadvantage of using a capillary is the limited accessibility of the inner surface for characterization and manipulation. In addition, optical refraction at the wall distorts the image when observing the contact angles. One of the main techniques for measuring dynamic contact angles has been to plunge or withdraw a plate,[4–6] cylinder,[7–11] fiber,[12,13] or tape[9,14–16] into or out off a liquid tank. Either the height of the meniscus is measured[4,6,10] or dynamic contact angles are obtained by imaging the contour of the meniscus.[8,11,13,14] A variety of materials with smooth surfaces can be used as plates or cylinders. The above techniques suffer from limitations concerning the range of realisable speeds or a limited choice of substrate materials. To circumvent these limitations we used an alternative technique: a rotating cylinder or drum.[17] In this method a horizontal cylinder is half immersed in the liquid. When rotating it at a defined velocity on one side the dynamic advancing contact angle is observed, on the other side the dynamic receding contact angle can be measured. The rotating cylinder allows a continuous observation of the three-phase contact line over a wide range of wetting/dewetting speeds. One should, however, keep in mind, that the immersion time and the "dry" time (*i.e.*, the time the surface is not immersed) are linked to the velocity and size of the cylinder. To achieve a steady state of the cylinder surface a prolonged rotation in the bath is necessary.

Several theories,[18–20] such as the molecular kinetic theory,[21] describe dynamic wetting. They in particular link the observed dynamic contact angles to the wetting speed. The standard description of dynamic contact angles, the hydrodynamic theory, assumes a balance of viscous and capillary forces near the contact line.[22–27] Hydrodynamic theory has been successfully applied to describe forced dewetting for a wide intermediate range of capillary numbers.[9,24,26,28] It often fails at very slow velocities of the order of $\mathrm{Ca} \leq 10^{-4}$.[5,6,10,29] At high velocities, of the order of $\mathrm{Ca} \geq 10^{-2}$,[10,11,30,31] typically the contact line becomes unstable and a continuous liquid film – called the Landau–Levich film – is formed.[11,32–34] Often, the instability of the receding contact line occurs by formation of a V-shaped corner.[15,31,35]

In hydrodynamic theory, a microscopic regime extending over a distance λ around the moving contact line is separated from a macroscopic flow regime. In the microscopic regime, slip between the liquid and the solid surface is allowed. For the apparent dynamic contact angle Θ the two regimes can be matched leading to:[9,24,26,28]

$$\Theta^3 = \Theta_0^3 \pm 9\mathrm{Ca}\ln\left(\frac{\alpha h}{\lambda}\right) \quad (2)$$

Here, Θ_0 is the contact angle obtained for velocity U close to zero ($U \to 0$). The sign is positive for advancing contact angles (for which eqn (2) was originally derived) and negative for receding contact angles (for which it turned out to be also applicable); here we consider the later. The numerical constant α depends on details of the specific geometry and on whether the receding or advancing situation is considered. The characteristic macroscopic length scale h is also given by the specific geometry. For a vertical plate the capillary constant $\kappa = \sqrt{\gamma_L/\rho g}$ is an appropriate choice for h; ρ is the density of the liquid and g = 9.81 m s^{-2} is the acceleration of gravity. Eqn (2) was derived assuming low contact angles and originally for advancing contact lines. It was, however, shown that it is also valid for contact angles up to 100–150°.[13,36]

While the dynamic wetting of simple, one component liquids has been studied extensively, multi-component liquids, like surfactant solutions, are less understood. Surfactant molecules adsorbed at interfaces influence the dynamic behavior of the liquid. They change for example the hydrodynamic boundary condition at liquid–gas interfaces[37–39] or the flow profile inside a liquid with a free surface.[40,41] Surfactants are used to control the extent of wetting/dewetting, due to their ability to reduce liquid–solid contact angles or to allow an aqueous solution to spread on non-polar surfaces.[42–47] The presence of surfactants increases the thickness of a film when withdrawing a fiber[48,49] or plate[40,50] from an aqueous solution. Luokkala *et al.* observed a decrease of the critical velocity when withdrawing a silicon wafer from aqueous solutions of nonionic surfactants poly(ethylene glycol)-monododecyl ether ($C_{12}E_n$).[51] Most studies concentrate on the thickness of the Landau–Levich films[40,48,52] but not directly on the velocity-dependent contact angles.

Previous studies showed that the cationic surfactant cetyl trimethylammonium bromide (CTAB) has a strong influence on the dynamic contact angle.[53,54] Also the critical velocity for film formation is drastically reduced. The effect was tentatively explained by the formation of local surface tension gradients close to the three-phase contact line, and therefore Marangoni tensions. When a surface is removed from a liquid bath fresh liquid–air interface is continuously formed close to the three-phase contact line (Fig. 1). Since this freshly created interface is not immediately covered with surfactant molecules, surface tension gradients, so called Marangoni tensions, arise.[48,49,55,56] These Marangoni tensions can slow down the liquid outflow of the region close to the three-phase contact line (purple arrow in Fig. 1).

The aim of the present manuscript is to demonstrate the generality of the surfactant-induced changes in the receding contact angle of surfactant solutions. Which observations are specific to CTAB and which one also hold for other surfactants? Do electrostatic effects play a role? What are the fundamental physical properties dominating forced dewetting? To answer these questions we vary the type of surfactant (anionic, cationic, nonionic) and the critical micelle concentration (CMC) of the surfactants (more than four orders of magnitude). For a set of representative surfactants we measured dynamic contact angles using a rotating cylinder setup. We demonstrate that the change in dewetting behavior is a universal phenomenon, occurring for all surfactants. We further analyze the flow profile near the receding contact line with and without surfactant. The velocities applied in this paper varied from 1 mm s^{-1} up to 200 mm s^{-1}.

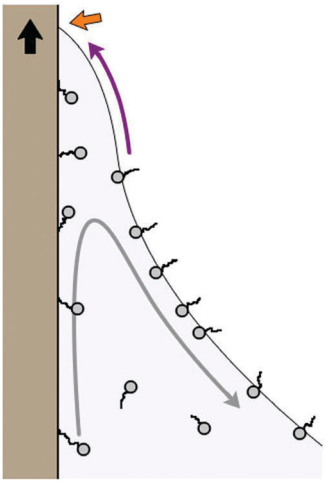

Fig. 1 Schematic microscopic picture of the region around the three-phase contact line of a surface drawn out of a liquid pool. The gray arrow indicates the liquid flow, while the surface is pulled upwards (black arrow) and fresh liquid–air interface is created (orange arrow). This fresh interface has a lower surfactant concentration, leading to a Marangoni tension slowing down the liquid flow (purple arrow).

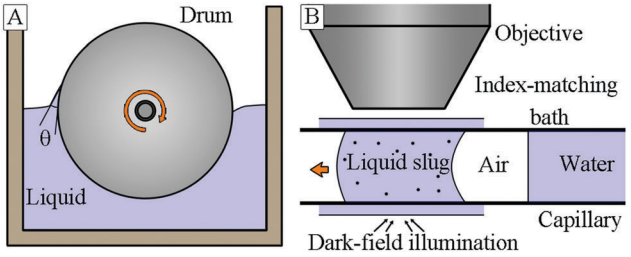

Fig. 2 (A) The rotating cylinder setup in side view to measure the contact angle and track the particle flow inside a dewetting liquid. (B) The micro tubing setup for measuring flow profiles close to the three-phase contact line using a liquid slug flowing through a capillary.

They are faster than Langmuir–Blodgett coating but slower than Landau–Levich film formation of pure water.[32] In the case of Landau–Levich film formation, added surfactants change qualitatively the flow profile.[41] In our experiments, the flow profile remains qualitatively the same. Both observations support the hypothesis that a Marangoni effect close to the three-phase contact line can account for the sharp decrease of dynamic receding contact angles.

Experimental section

Materials

Anionically polymerized polystyrene (M_W = 300 kg mol^{-1}) and tetrahydrofuran (THF, Sigma-Aldrich) were used without further purification. Cetyl trimethylammonium bromide (CTAB, $[(C_{16}H_{33})N(CH_3)_3Br]$, cationic) was purchased from Sigma-Aldrich, sodium 1-decanesulfonate (S-1DeS, $C_{10}H_{21}SO_2OHNa$, anionic) from Sigma-Aldrich and butyl glycol (C_4E_1, $C_4H_9OCH_2CH_2OH$, nonionic) from Alfa Aesar. Octyltriglycol (C_8E_3, $C_8H_{17}(OCH_2CH_2)_3OH$, nonionic) and dodecyl pentaglycol ($C_{12}E_5$, $C_{12}H_{25}(OCH_2CH_2)_5OH$ nonionic) were purchased from Sigma-Aldrich. All surfactants were used without further purification. Milli-Q water was prepared by purifying water using an Arium® 611 ultrapure water system (Sartorius) or Arium® pro VF/UF&DI/UV (Sartorius) at a resistivity of 18.2 MΩ cm.

Rotating cylinder setup

The rotating cylinder setup consists of an exchangeable stainless steel cylinder horizontally mounted in a bath filled with water or a surfactant solution, up to the axis (Fig. 2A).[53,54] The bath has a width of 10 cm, a depth of 17 cm and a height of 15 cm. The cylinder has a diameter of 12 cm. Its spherical segment geometry allowed for a precise imaging and thus accurate measurement of the contact angle. The cylinder was coated with polystyrene by rotating it at a speed of 100 mm s^{-1} in a 0.8 wt% solution of polystyrene in THF (tetrahydrofuran). After 5 min the solution was quickly removed, resulting in a polystyrene film on the cylinder. This film was first dried at room temperature and then for 16 h at 60 °C. The advancing and receding contact angles of water measured with a sessile drop on the surface were 66° and 100°, respectively. Scanning force microscopy (SFM, JPK NanoWizard™, Berlin, Germany) was used to measure the roughness of the cylinder coating. The SFM measurements were performed in tapping mode (cantilever: Olympus OMCL-AC240TS, spring constant 2 N m^{-1}, resonance frequency 70 kHz, in air at room temperature) directly on the cylinder surface. The latter was realized by building a special scaffold where the SFM head was placed. The surface roughness measured and analyzed using Gwyddion software over areas of 50 × 50 μm^2 was in the order of 150 nm, mainly caused by the underlying polished steel.

For measuring the contact angle brightfield microscopy with a high speed camera (Photron, Fastcam SA-1, 12× magnification, working distance about 30 cm, 250–500 frames per s) was used. The contact angle was determined by fitting straight line to the solid surface and to the liquid–air interface at the point where both meet. All experiments were carried out at a temperature of 21 °C in a closed bath with water saturated atmosphere. For cleaning the setup between the measurements the setup was first placed for several hours under flowing tap water and then rinsed for 1 h under flowing Milli-Q water. As an indication for clean conditions we took the fact that in pure water the contact angles were constant and did not change with time. The error in contact angle was ≈5° from one experiment to another and ≈3° within one series of experiments. For contact angle below 15° the error slightly increases.

For visualizing the flow profile in the rotating cylinder setup, small amounts of silica particles (0.05 wt%, Kromasil 100, diameter 10 ± 2 μm, Analysentechnik Mainz) were dispersed in the liquid. The particle movement was detected by using a macro-zoom optics (12× magnification) equipped with a fast camera (Photron, Fastcam SA-1, 1000 frames per s). The flow profile of the liquid was measured by analyzing the particle trajectories making use of the particle tracking plugin of ImageJ.

Table 1 Critical micelle concentrations (CMCs), the surface tensions at high concentration γ^*, diffusion coefficients D at 25.1 °C, and molar masses M_W for the different surfactants

Surfactant	Type	CMC (mM)	γ^* (mN m^{-1})	D (m^2 s^{-1})	M_W (g mol^{-1})
C_4E_1	Nonionic	1.2×10^3	27.9	9.3×10^{-10}	118
C_8E_3	Nonionic	7.5	27.3	4.6×10^{-10}	262
$C_{12}E_5$	Nonionic	7.0×10^{-2}	30.7	2.9×10^{-10}	407
CTAB	Cationic	1.0	35.2	5.4×10^{-10}	364
S-1DeS	Anionic	38.5	38.7	7.0×10^{-10}	244

Surfactant solutions

Before surfactant was added to the bath the dynamic contact angles of pure water were measured. After adding the surfactant, the solutions were stirred for at least 20 min by rotation the cylinder at a constant speed of 100 mm s^{-1}. Surfactant was stepwise added to achieve concentrations of up to 30% of the respective CMC. The CMCs and the surface tensions of aqueous solutions at the CMCs are summarized in Table 1. The surface tensions were measured with a Wilhelmy plate tensiometer (Dataphysics, DCAT 11EC). CMCs were extracted from a plot of surface tension *versus* log of concentration (Fig. S1, in ESI†). The measured CMCs agree with values reported in the literature.[57,58]

NMR spectroscopy

For the ^{1}H-NMR experiments and the diffusion measurements (DOSY)[59] a 5 mm triple resonance TXI ^{1}H/^{13}C/^{15}N probe equipped with a z-gradient on the 850 MHz Bruker AVANCE III system was used. For the diffusion measurements a 2D sequence (DOSY, stebpgp1s19) with a stimulated echo was used additionally with water suppression (3-9-19 pulse sequence with gradients).[60] The temperature was kept at 25.1 °C and regulated by a standard ^{1}H methanol NMR sample using the topspin 3.1 software (Bruker). The control of the temperature was realized with a VTU (variable temperature unit) and an accuracy of ±0.1 K. In this work, the gradient strength was varied in 16 steps from 2% to 100%. The diffusion time was optimised at 30 ms and the gradient length to 1.2 ms. The gradient strength was calibrated by analysis of a sample of $^2H_2O/^1H_2O$ and comparison with the theoretical diffusion coefficient of $^2H_2O/^1H_2O$. Diffusion gradient amplitudes were varied linearly from 1 to 53 G cm^{-1} (10 to 470 mT m^{-1}) over a total of 16 experiments to achieve a strong diffusion weighting. Diffusion coefficients were calculated for the integrated peak areas using an exponential decay fit function over the 16 spectra: $S_i = S_0 \exp(-Db_i)$. Here, the diffusion sensitivity factor b was calculated as given in the sequence description: $b_i = (2\pi g_L G_i d)^2(\Delta - d/3)$, where g_L is the gyromagnetic ratio of the observed nucleus, G_i is the gradient strength, d is the length of the gradient (1.2 ms), and Δ is the diffusion time (30 ms).

Microtubing setup

Due to reflections from the air–liquid interface, the flow closer than ≈300 μm to the undeformed interface and in the updrawn liquid meniscus could not be visualized in the rotating cylinder experiments. To visualize the flow close to the three-phase contact line, we therefore used a different experimental setup based on a microtube (Fig. 2B).[61] A glass beaker containing milli-Q water was placed on a translation stage. The beaker was connected to a capillary (inner diameter 855 μm) through a tubing system and a metering valve. The capillary, mounted in a homemade flat glass cell, was placed on the stage of an upright optical microscope (Olympus BX 51). All tubes were made from fluorinated ethylene propylene (FEP) (Bohlender, Germany). The mean surface roughness of the thin capillary was 50 nm, measured with confocal microscopy (μ-Surf, Nano-Focus). To avoid light distortion due to the cylindrical geometry of the FEP capillary (refractive index n = 1.34), the glass cell was filled with water (n = 1.33).

Liquid slugs containing carboxylated polystyrene microparticles (Kisker Biotech, Germany) of 4 μm diameter at a concentration 0.05% wt were introduced in the fluidic system using a syringe. The driving force for the slug motion is the pressure drop generated between the elevated beaker and the capillary outlet. Control of the flow speed was achieved by adjusting the height of the water level in the beaker as well as by regulating the metering valve. Transmission microscopy videos of the slug motion under dark field illumination conditions were captured by means of a 10× objective and a fast CMOS camera (Olympus i-speed, maximum frame rate 2000 frames per s). Before the flow visualization experiments the whole setup was carefully cleaned by flushing 150 mL acetone and 150 mL milli-Q water. Before each single measurement, the FEP capillaries were independently washed with ≈20 mL acetone and were subsequently completely dried using flowing N_2. This procedure was found to provide clean surfaces, an essential requirement for reproducible results.[61]

Results and discussion

Pure water

To describe the dewetting behavior we plotted the apparent receding contact angles Θ (when the cylinder leaves the liquid) *versus* the rotation velocity at the cylinder surface. For pure water the receding contact angles decreased with increasing rotation velocity (Fig. 3, open circles). When approaching a velocity of 200 mm s^{-1} (Ca = 2.7×10^{-3}) a triangular or V-shaped liquid film was formed spanning the whole width of the cylinder (as described in ref. 53). This change in the shape of the contact line made it difficult to measure the contact angle and we stopped at this velocity. At even higher speeds (U > 200 mm s^{-1}) a trail of drops formed at the upper corner of the triangle and remained on the surface of the cylinder. Such V-shaped contact lines and "pearling drops" were observed before[15,30,62] and their shape has been calculated.[63] At even higher speeds, we observe the transition from a defined three-phase contact line to the entrainment of a liquid film, known as the Landau–Levich–Derjaguin transition.[11,32–34] Above this critical velocity a continuous liquid film is drawn upwards.

Aqueous surfactant solutions

When adding surfactant, qualitatively the same phases were observed: a relatively straight, horizontal contact line at low

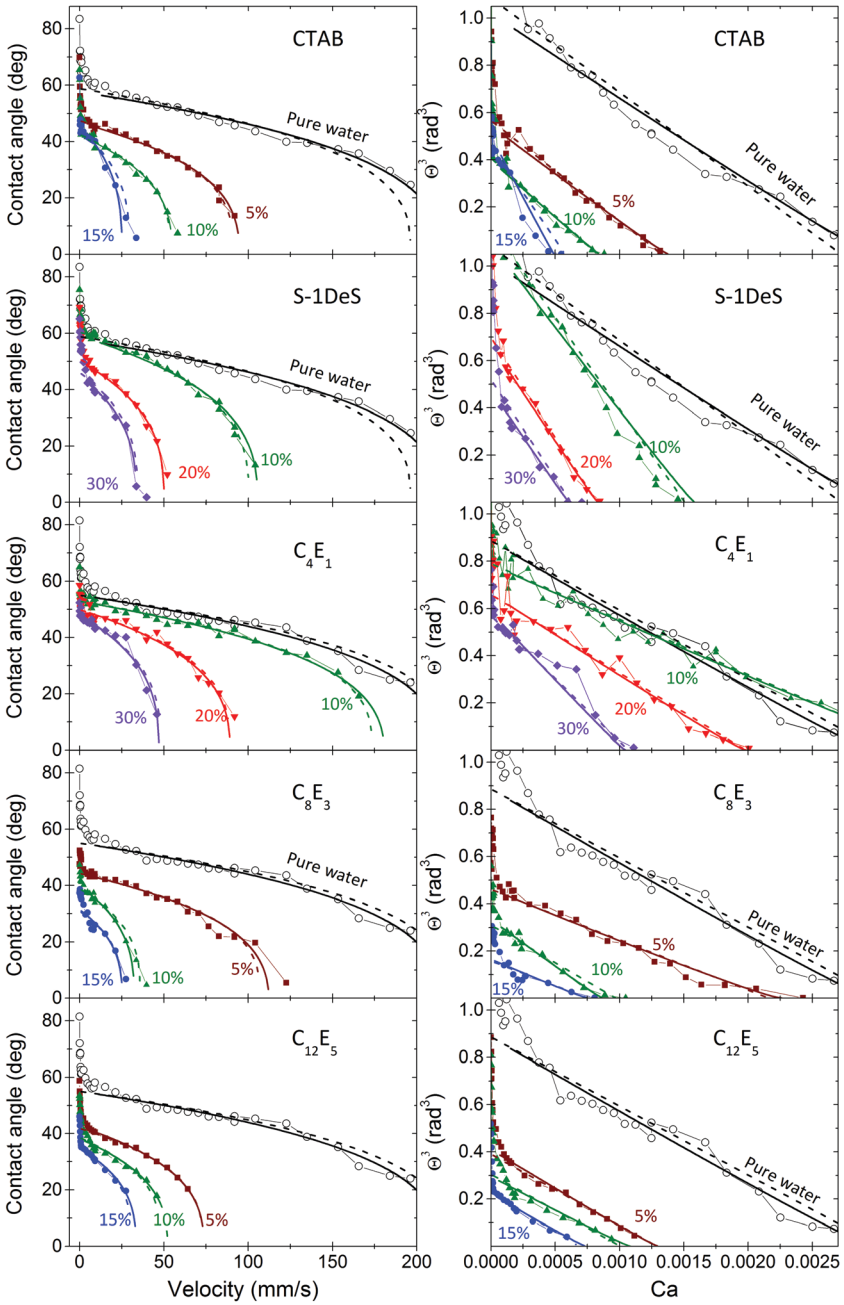

Fig. 3 Left: Dynamic receding contact angle of aqueous solutions *versus* velocity for the surfactants CTAB (cationic), S-1DeS (anionic), and C_4E_1, C_8E_3, $C_{12}E_5$ (nonionic) on a polystyrene-coated cylinder. Right: Contact angle (in rad) cubed *versus* the capillary number $Ca = \eta U/\gamma_L$. Here, $\eta = 10^{-3}$ Pa s is the viscosity of water. Results for pure water are indicated by open black circles. The concentrations (in % of CMC) were 5% (dark red circles), 10% (green up triangles), 15% (blue circles), 20% (light red down triangles), and 30% (violet diamonds). For pure water we only show two independent measurements; the top two and the bottom three results for pure water are identical. The solid lines are fits using eqn (3), the dashed line are fits using eqn (2).

velocity, formation of a triangular shape at intermediate velocity and formation of a continuous film at high velocity. At our optical resolution we were not able to see micrometer sized distortions as reported by Varanasi & Garoff.[45]

Quantitatively, however, the picture changed when adding surfactant (Fig. 3):

- The slopes of the graphs Θ *vs.* U became steeper.
- As a result, the critical velocity for film formation decreased with increasing surfactant concentration.
- The apparent receding contact angle for zero velocity $\Theta(U \to 0)$ decreased.

The described behavior was observed for all types of surfactants at roughly the same relative concentration (in %CMC). This holds even when changing the absolute surfactant concentration by more than four orders of magnitude. This similarity indicates that the reason for the decreasing dynamic contact angle effect is universal and does not depend on the specific length of the hydrocarbon chain or the specific structure of the

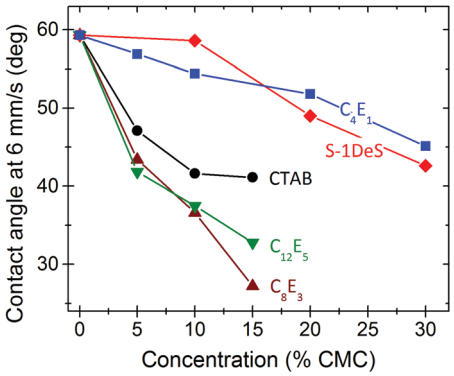

Fig. 4 Dynamic receding contact angles at a velocity of 6 mm s^{-1} *versus* surfactant concentration, for all surfactants used. Surfactant concentrations are given in percentages of the CMC.

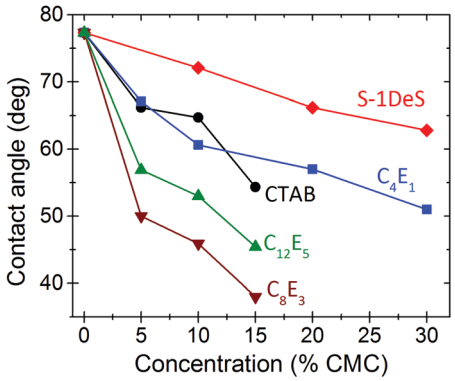

Fig. 5 Apparent receding contact angles *versus* concentration for the five surfactants used. The concentration is scaled by dividing the actual concentration by the CMC of the respective surfactant. The values reported are mean values for zero velocity and the first data point for the slowest velocity of typically 0.14 mm s^{-1}. The error, estimated from multiple experiments with pure water, is ≈3°.

hydrophilic head group. In particular, the charge of the surfactant does not play a role, which excludes electrostatic interactions as a major explanation for the observed decrease in contact angle.

To compare the different surfactants we looked into the dynamic contact angles at one fixed velocity (Fig. 4, velocity 6 mm s^{-1} and Fig. S2, 20 mm s^{-1} in ESI†). While the CMCs of the surfactants varied over more than four orders of magnitude (Table 1) the dynamic contact angles differed only by a factor three. The effect of scaling with the CMC is also evident, when plotting the contact angle *versus* the concentrations in mM, irrespective of the velocity (Fig. S3, ESI†). After scaling the concentrations with their respective CMCs, C_8E_3 and $C_{12}E_5$ are the two most effective surfactants. C_4E_1 and S-1DeS require a roughly three times higher concentration to reach the same dynamic contact angle.

The fact that dynamic contact angles of all surfactant solutions are roughly the same at the same relative concentration (Fig. 4) is the most important finding. Scaling all concentrations by the CMC allows us to predict the dynamic contact angle of all surfactants. The remaining differences between different surfactants will be discussed below.

Receding contact angle for zero velocity

The receding contact angle for $U \rightarrow 0$ decreased with increasing surfactant concentration for all surfactants (Fig. 5). That surfactants decrease the contact angle of aqueous solutions on hydrophobic surface is known.[46,64–66] For a guideline in the interpretation we apply Young's eqn (1). For pure water the receding contact angle was 77°. With γ_L = 72.1 mN m^{-1} at zero surfactant concentration Young's eqn (1) leads to $\gamma_S - \gamma_{SL}$ = 16.2 mN m^{-1}. The decreasing contact angle can only be explained by assuming that surfactant adsorb at the solid–air and/or solid–liquid interface. The argument is: if there were no adsorption at the solid surface nor at the solid–liquid interfaces, $\gamma_S - \gamma_{SL}$ would be constant. Keeping $\gamma_S - \gamma_{SL}$ = 16.2 mN m^{-1} constant and inserting the measured values for γ_L in Young's equation leads to contact angles, which are too high, *e.g.* the lowest contact angle obtained within this assumption would be 61° for C_8E_3 at 15 %CMC. All other surfactants would have even higher contact angles between 69° and 75°. The actually observed contact angles are significantly lower and consequently in contradiction our non-adsorption assumption. Thus, $\gamma_S - \gamma_{SL}$ increases. Please note, we used the measured values for γ_L since γ_L decreases when adding surfactant.

Processes influencing the Marangoni effect

Surfactants adsorb to the relatively hydrophobic polystyrene surface much like they adsorb to the liquid–air interface.[46,67] When the contact line recedes, the adsorbed surfactants have two possibilities: they remain on the solid surface (process 1 in Fig. 6) or they transfer to the new liquid–air interface (process 2); to directly diffuse back into the bulk is unlikely. The less surfactant transfers to the freshly created liquid–air interface, the higher the gradient in surface tension and the Marangoni stress. The more surfactants transfer to the liquid–air interface, the lower the gradient in interfacial tension.[51] The fact that we

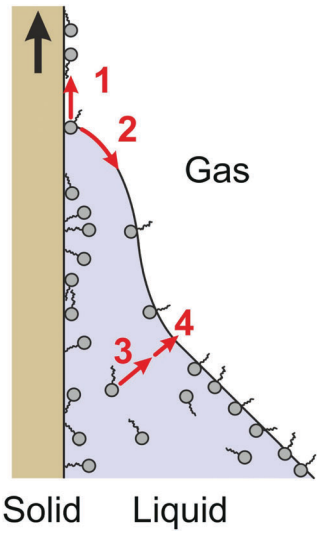

Fig. 6 Schematic of processes at the receding contact line. Details are explained in the main text.

observe a Marangoni effect again indicates that the transferred surface concentration is lower than the equilibrium surface concentration at the given bulk concentration.

Once a fresh liquid surface has been formed at the contact line, the surface tension gradient is equilibrated by surfactants from the bulk. The transfer rate of surfactant to the liquid–air interface involves two steps: advection and diffusion from the bulk (process 3) and adsorption to the liquid–air interface (process 4). It is noteworthy that C_4E_1 and S-1DeS need slightly higher concentrations to achieve the same reduction in contact angle as the other surfactants (Fig. 4 and 5). They are the smallest molecules and they have the fastest diffusion coefficient (Table 1). Therefore, the faster diffusion may lead to a faster equilibration of the surface tension gradient. However, since at the same time the total concentration is much higher than for the other surfactants, one should be careful drawing conclusions. The differences remaining after scaling the dynamic receding contact angles with the CMCs could be due to any of the processes 1–4 described or a combination. At present we cannot link the remaining differences to one specific process.

Comparison of experimental results with hydrodynamic theory

For velocities above $\approx$10 mm s^{-1} (Ca $\approx 10^{-4}$) experimental results could be fitted with the Cox–Voinov law eqn (2) (dashed lines in Fig. 3). In the presence of surfactant hydrodynamic theory even fitted the results down to 1 mm s^{-1}. This agreement is best visualized by plotting Θ^3 *vs.* Ca (Fig. 3, right), in which eqn (2) leads to straight lines. Hydrodynamic theory fitted all Θ *vs.* U curves up to the point, where the liquid film formed a triangular shape. Therefore, two velocity regimes could be distinguished: strongly decreasing contact angle for low velocities and a more gradual decrease of the apparent dynamic contact angle for velocities above $\approx$10 mm s^{-1}. The fast part is well described by hydrodynamic theory.

Snoeijer & Andreotti[68] point out that eqn (2) was derived for advancing, not for receding contact angles. An approximate solution for receding contact lines was derived by Eggers[27] assuming a small Θ_0. To test the difference between both approaches, we also fit with the full equations valid for the receding contact lines. Eggers & Snoeijer[27,69] showed that the apparent receding contact angle Θ follows

$$\frac{\Theta}{\Theta_0} = \frac{2^{2/3}\delta^{1/3}}{\mathrm{Ai}(\sigma)} \left.\frac{\mathrm{dAi}(x)}{\mathrm{d}x}\right|_{x=\sigma} \qquad (3)$$

Here, $\delta = 3\mathrm{Ca}/\Theta_0{}^3$ and all lengths are rescaled using the capillary length. σ is the largest root of[27,69]

$$\frac{2}{\Theta_0\delta^{1/3}} + \frac{2^{2/3}}{\mathrm{Ai}(\sigma)} \left.\frac{\mathrm{dAi}}{\mathrm{d}x}\right|_{x=\sigma} - \frac{2^{1/6}e^{-1/(3\delta)}\Theta_0}{3\pi\mathrm{Ai}^2(\sigma)\lambda} = 0 \qquad (4)$$

Here Ai and dAi/dx is the Airy function and its first derivative, respectively. This model also contains two adjustable parameters: the length of the microscopic regime λ and the contact angle at zero velocity Θ_0. All other parameters can be determined independently.

At this point a more detailed description of the numerical implementation of the theory is instructive. Eqn (3) and (4) were implemented in Matlab. In all investigated cases eqn (3) had only one positive root. So the root finding was found to be numerically stable when limiting the range of σ to not so large positive numbers, typically $\sigma < 60$. To perform the nonlinear fit for the unknown parameters λ and Θ_0 it turned out to be more efficient to take the logarithm of λ as a fit parameter. Like for all nonlinear fits, the quality of the fit is only good, when the initial guesses of the parameters are not too far away from the final value. For the two parameters "not too far away" was not more than about $\pm$20 for the logarithm of λ and a factor of about 1.5 for Θ_0. When initial guesses are chosen within this range, the final values do not depend on the initial guesses. The fits to eqn (2) were performed with the built-in routines of Origin.

A simple interpretation of the two parameters goes as follows: Θ_0 is the apparent receding contact angle when extrapolating the high velocity branch of the dynamic contact angle measurements to zero velocity: $\Theta_0 = \Theta(U \to 0)$. This is not the equilibrium contact angle. The logarithm of the microscopic parameter $\alpha h/\lambda$ (in eqn (2)) and $1/\lambda$ (in eqn (3) and (4)) measures friction close to the contact line. The different prefactor to λ is due to the rescaling of all length in eqn (3) and (4). The higher this "friction parameter" the more energy is dissipated close to the contact line, *e.g.* by hydrodynamic dissipation. Note that close to the contact line surface tension gradients (due to the presence of surfactants) might alter the flow profile. Without going into the details of the changes in the flow profile, we assume that ultimately, such changes will increase the hydrodynamic dissipation close to the contact line. In our model the details of the flow profile close to the contact line are not taken into account and only summarized in changes in the friction parameter.

To identify potential differences between the simple hydrodynamic model of eqn (2) and the more developed model of eqn (3) and (4) we fitted our experimental data with both models. Despite the fact that eqn (2) should only be valid for advancing contact lines,[68] our data can be fitted with eqn (2). Neither the quality of the fit nor the absolute numbers of the fit parameters showed significant differences between the two approaches (Fig. 7).

The friction coefficient is relatively constant for nonionic surfactants (Fig. 7). Up to 15% CMC we did not observe a significant change with concentration. For C_4E_1, which was the only nonionic surfactant studied at higher relative concentration, friction tends to increase for $c > 15\%$. For the two charged surfactants the friction parameter increased with increasing concentration. This can also be directly seen from the linear fits of Θ^3 on the left side of Fig. 3: while for CTAB and S-1Des the slope of the plots increased, for the neutral C_8E_3 and $C_{12}E_5$ curves are primarily shifted downwards. Such a downward shift is reflected in a strongly decreasing value for Θ_0 (Fig. 7B). We speculate that the high friction parameter of the two ionic surfactants is due changes in the adsorption kinetics caused by electrostatic repulsion. The second step (process 4, Fig. 6), adsorption, is slowed down by electrostatic repulsion between surfactant molecules close to the surface and those already adsorbed.[70]

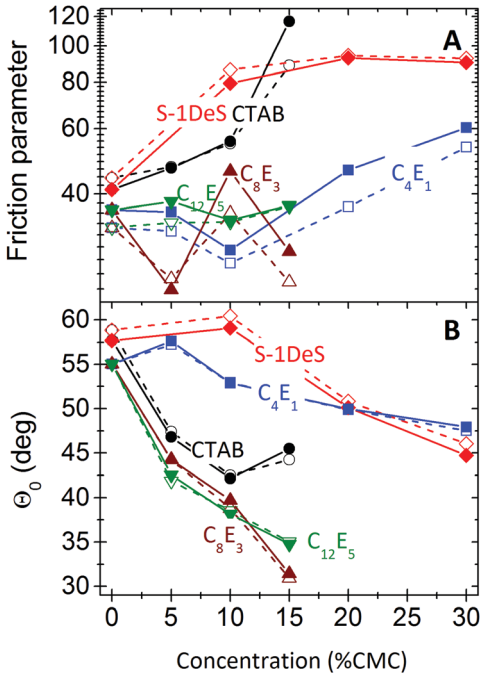

Fig. 7 Friction parameter λ (top) and contact angle extrapolated to zero velocity Θ_0 (bottom) obtained from fitting experimental results with eqn (2) (open symbols) and with eqn (3) and (4) (solid symbols) plotted as a function of the concentration of surfactant. The concentration is scaled by dividing the actual value by the CMC of the respective surfactant. The error estimated from different experiments for pure water is of the order $\approx$20% and 3°, respectively.

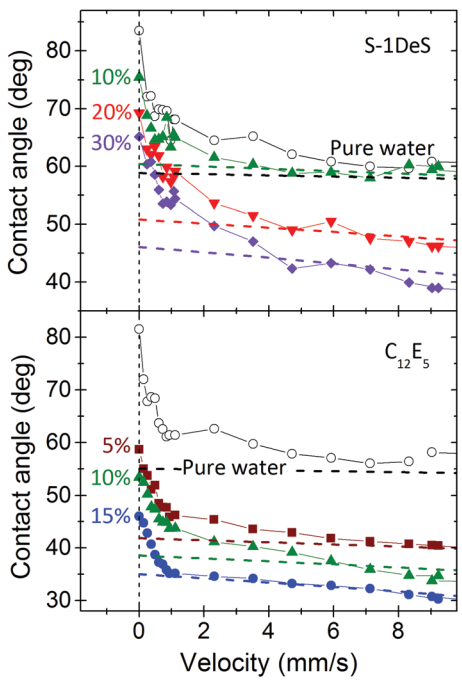

Fig. 8 Dynamic receding contact angle *versus* velocity for S-1DeS and $C_{12}E_5$ measured at different surfactant concentrations. The dashed lines represent the hydrodynamic fits obtained with eqn (2) for $U > 10$ mm s^{-1}. The concentration is scaled by dividing the actual value by the CMC of the respective surfactant. For pure water the results of two different experiments are shown.

Decrease of the contact angle at slow velocity

The decrease of dynamic contact angles with contact line velocity follows two phases, a slow and a fast. Hydrodynamic theory fits well the contact angles at velocities above 5–10 mm s^{-1}. It does not fit the slow component. As an example, Fig. 8 shows the slow change for two representative surfactants. Below a typical velocity of $\approx$1–5 mm s^{-1} (Ca ≈ 1.4–7×10^{-5}), Θ *vs.* U decreases more steeply than at higher velocities. For pure water the slow regime even extends to $U \approx 10$ mm s^{-1} (Ca $\approx 1.4 \times 10^{-4}$), as can be seen from the fact that experimental results are still above the hydrodynamic fit up to 10 mm s^{-1}.

When comparing changes in receding contact angle for pure water and different surfactant concentrations for slow velocities ($U \leq 5$ mm s^{-1}) the curves Θ *vs.* U look very similar. We take this as an indication that the major reason for this decrease at

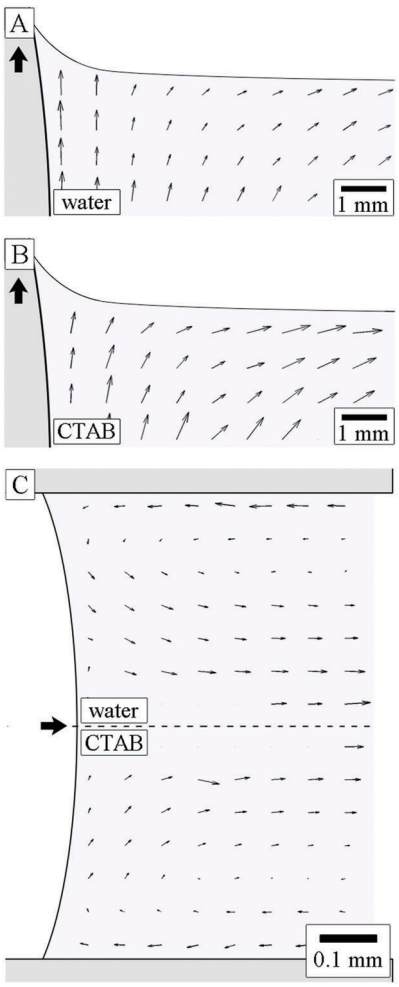

Fig. 9 Flow profiles indicated by arrows as measured at a rotation velocity of 20 mm s^{-1} for the rotating cylinder setup with (A) pure water and (B) a 10% CMC CTAB solution. Flow profiles did not differ significantly. (C) To visualize the flow closer to the three-phase contact line, a liquid slug in a capillary was examined at a flow velocity of about 0.3 mm s^{-1}. The flow of either pure water (top) or 100% CTAB (bottom) did not change: the flow inside the capillary was symmetric with vortices close to the walls. Arrows indicate the direction of the movement: (A and B) rotation direction, (C) flow direction.

slow velocity is not the Marangoni effect but that it is due to another, yet unidentified process, *e.g.* the small but finite roughness of the cylinder.

Flow profiles near the contact line

Tracer particles added to the rotating cylinder setup allowed to visualize the flow in pure water and CTAB solution (Fig. 9A and B). The flow observed in pure water resembles the one of pure water observed for the Landau–Levich flow and is compatible with the standard hydrodynamics of receding contact lines: close to the solid–liquid interface the water is drawn upwards. It changes direction near the three-phase contact line and flows downwards close to the liquid–air interface (Fig. 9A).

In CTAB solution the overall flow profile in the bulk liquid did not change significantly. This is in contrast to the Landau–Levich flow where the presence of surfactant molecules fundamentally change the flow profile.[41]

The flow of water inside the capillary close to the liquid–air interface was symmetric and showed two vortices. The flow profile did not change when adding CTAB (Fig. 9C; top: water, bottom: CTAB). Also variations of the absolute value of the flow velocity did not influence the flow profiles close to the contact line, as long as the critical velocity of complete wetting was not exceeded.

Conclusions

The dynamic receding contact angle of aqueous solution changes significantly when adding surfactant. For all surfactant solutions (C_4E_1, C_8E_3, $C_{12}E_5$, S-1DeS, and CTAB) the receding contact angles decreased with increasing velocity as well as with increasing surfactant concentration. The Marangoni stresses seem to have the main contribution to the contact angle decrease: local surface tension gradients formed close to the three-phase contact line influencing the liquid flow along the liquid–air interface while not significantly influencing the flow profile in the bulk liquid. By comparing the results of changes in the contact angle in % of CMC we shown that the charge of the surfactant has no significant influence on the wetting behavior. The relative concentration is (in %CMC) by far the dominating parameter for the receding contact angle even for surfactants which change by more than four orders of magnitude in the CMC. The dominating scaling parameter is the CMC. This allows to give predictions of the effect for other surfactants as well. For high enough dewetting speed (>10 mm s^{-1}), the hydrodynamic models fit the experimental data well. In the hydrodynamic model all local effects close to the contact line can be summarized in a friction parameter similar to the dewetting of simple liquids.

Acknowledgements

It is a pleasure to acknowledge financial support by the ERC Advanced grant SUPRO 340391 (H. J. B.) and by the European Marie Curie Initial Training Network COWET (G. A., H. J. B.). T.-H. N. thanks the SFB 625 and IMPRS for partial financial support. We gratefully acknowledge the support of Uwe Rietzler and Rüdiger Berger for designing and building the scaffold for the SFM measurements.

References

1 T. Young, *Philos. Trans. R. Soc. London*, 1805, **95**, 65–87.
2 W. Rose and R. W. Heins, *J. Colloid Sci.*, 1962, **17**, 39–48.
3 R. L. Hoffman, *J. Colloid Interface Sci.*, 1975, **50**, 228–241.
4 J. B. Cain, D. W. Francis, R. D. Venter and A. W. Neumann, *J. Colloid Interface Sci.*, 1983, **94**, 123–130.
5 R. A. Hayes and J. Ralston, *J. Colloid Interface Sci.*, 1993, **159**, 429–438.
6 R. V. Sedev, C. J. Budziak, J. G. Petrov and A. W. Neumann, *J. Colloid Interface Sci.*, 1993, **159**, 392–399.
7 J. G. Petrov and B. P. Radoev, *Colloid Polym. Sci.*, 1981, **259**, 753–760.
8 E. B. Dussan, E. Ramé and S. Garoff, *J. Fluid Mech.*, 1991, **230**, 97–116.
9 P. G. Petrov and J. G. Petrov, *Langmuir*, 1992, **8**, 1762–1767.
10 R. V. Sedev and J. G. Petrov, *Colloids Surf.*, 1992, **62**, 141–151.
11 M. Maleki, E. Reyssat, D. Quéré and R. Golestanian, *Langmuir*, 2007, **23**, 10116–10122.
12 G. Inverarity, *Br. Polym. J.*, 1969, **1**, 245–251.
13 J. G. Petrov, J. Ralston, M. Schneemilch and R. A. Hayes, *J. Phys. Chem. B*, 2003, **107**, 1634–1645.
14 R. Burley and B. S. Kennedy, *Br. Polym. J.*, 1976, **8**, 140–143.
15 T. D. Blake and K. J. Ruschak, *Nature*, 1979, **282**, 489–491.
16 E. B. Gutoff and C. E. Kendrick, *AIChE J.*, 1982, **28**, 459–466.
17 R. Ablett, *Philos. Mag.*, 1923, **46**, 244–256.
18 Y. D. Shikhmurzaev, *Fluid Dynamics Research*, 1994, **13**, 45–64.
19 J. Billingham, *Eur. J. Appl. Math.*, 2006, **17**, 347–382.
20 A. Rednikov and P. Colinet, *Phys. Rev. E: Stat., Nonlinear, Soft Matter Phys.*, 2013, **87**, 010401.
21 T. D. Blake and J. M. Haynes, *J. Colloid Interface Sci.*, 1969, **30**, 421–423.
22 G. Friz, *Z. Angew. Phys.*, 1965, **19**, 374–378.
23 C. Huh and L. E. Scriven, *J. Colloid Interface Sci.*, 1971, **35**, 85–101.
24 O. V. Voinov, *Fluid Dyn.*, 1976, **11**, 714–721.
25 L. H. Tanner, *J. Phys. D*, 1979, **12**, 1473–1484.
26 R. G. Cox, *J. Fluid Mech.*, 1986, **168**, 169–194.
27 J. Eggers, *Phys. Fluids*, 2005, **17**, 082106.
28 J. G. Petrov and P. G. Petrov, *Colloids Surf.*, 1992, **64**, 143–149.
29 W. Hopf and H. Stechemesser, *Colloids Surf.*, 1988, **33**, 25–33.
30 T. Podgorski, J. M. Flesselles and L. Limat, *Phys. Rev. Lett.*, 2001, **87**, 036102.
31 I. Peters, J. H. Snoeijer, A. Daerr and L. Limat, *Phys. Rev. Lett.*, 2009, **103**, 114501.
32 L. Landau and B. Levich, *Acta Physicochim. URSS*, 1942, **17**, 42–54.
33 B. V. Derjaguin, *Acta Physicochim. URSS*, 1943, **20**, 349–352.

34 J. H. Snoeijer, J. Ziegler, B. Andreotti, M. Fermigier and J. Eggers, *Phys. Rev. Lett.*, 2008, **100**, 244502.
35 K. G. Winkels, I. R. Peters, F. Evangelista, M. Riepen, A. Daerr, L. Limat and J. H. Snoeijer, *Eur. Phys. J.: Spec. Top.*, 2011, **192**, 195–205.
36 M. Fermigier and P. Jenffer, *J. Colloid Interface Sci.*, 1991, **146**, 226–241.
37 Y. Amarouchene, G. Cristobal and H. Kellay, *Phys. Rev. Lett.*, 2001, **87**, 206104.
38 O. Manor, I. U. Vakarelski, X. S. Tang, S. J. O'Shea, G. W. Stevens, F. Grieser, R. R. Dagastine and D. Y. C. Chan, *Phys. Rev. Lett.*, 2008, **101**, 024501.
39 D. Y. C. Chan, E. Klaseboer and R. Manica, *Soft Matter*, 2009, **5**, 2858–2861.
40 R. Krechetnikov and G. M. Homsy, *J. Fluid Mech.*, 2006, **559**, 429–450.
41 H. C. Mayer and R. Krechetnikov, *Phys. Fluids*, 2012, **24**, 052103.
42 M. von Bahr, F. Tiberg and V. Yaminsky, *Colloids Surf., A*, 2001, **193**, 85–96.
43 V. Dutschk, K. G. Sabbatovskiy, M. Stolz, K. Grundke and V. M. Rudoy, *J. Colloid Interface Sci.*, 2003, **267**, 456–462.
44 V. M. Starov, M. G. Velarde and C. J. Radke, *Wetting and Spreading Dynamics*, CRC Press, London, 2007.
45 K. S. Varanasi and S. Garoff, *Langmuir*, 2005, **21**, 9932–9937.
46 B. P. Binks, A. J. Johnson and J. A. Rodriques, *Soft Matter*, 2010, **6**, 126–135.
47 J. Venzmer, *Curr. Opin. Colloid Interface Sci.*, 2011, **16**, 335–343.
48 D. Quéré, A. de Ryck and O. O. Ramdane, *Europhys. Lett.*, 1997, **37**, 305–310.
49 Q. Shen, B. Gleason, G. H. McKinley and H. A. Stone, *Phys. Fluids*, 2002, **14**, 4055–4068.
50 D. M. Campana, S. Ubal, M. D. Giavedoni and F. A. Saita, *Phys. Fluids*, 2010, **22**, 032103.
51 B. B. Luokkala, S. Garoff, R. D. Tilton and R. M. Suter, *Langmuir*, 2001, **17**, 5917–5923.
52 D. Quéré, *Annu. Rev. Fluid Mech.*, 1999, **31**, 347–384.
53 D. Fell, G. Auernhammer, E. Bonaccurso, C. J. Liu, R. Sokuler and H. J. Butt, *Langmuir*, 2011, **27**, 2112–2117.
54 D. Fell, N. Pawanrat, E. Bonaccurso, H.-J. Butt and G. K. Auernhammer, *Colloid Polym. Sci.*, 2013, **291**, 361–366.
55 L. E. Scriven and C. V. Sternling, *Nature*, 1960, **187**, 186–188.
56 C. W. Park, *J. Colloid Interface Sci.*, 1991, **146**, 382–394.
57 M. J. Rosen, A. W. Cohen, M. Dahanayake and X. Y. Hua, *J. Phys. Chem.*, 1982, **86**, 541–545.
58 A. Paszternák, É. Kiss and P. Jedlovszky, *J. Chem. Phys.*, 2005, **122**, 124704.
59 E. O. Stejskal and J. E. Tanner, *J. Chem. Phys.*, 1965, **42**, 288.
60 A. Jerschow and N. Müller, *J. Magn. Reson.*, 1997, **125**, 372–375.
61 M. Anyfantakis, D. Fell, H.-J. Butt and G. K. Auernhammer, *Chem. Lett.*, 2012, **41**, 1232–1234.
62 G. Delon, M. Fermigier, J. H. Snoeijer and B. Andreotti, *J. Fluid Mech.*, 2008, **604**, 55–75.
63 J. H. Snoeijer, N. Le Grand-Piteira, L. Limat, H. A. Stone and J. Eggers, *Phys. Fluids*, 2007, **19**, 042104.
64 M. K. Bernett and W. A. Zisman, *J. Phys. Chem.*, 1959, **63**, 1241–1246.
65 V. M. Starov, S. R. Kosvintsev and M. G. Velarde, *J. Colloid Interface Sci.*, 2000, **227**, 185–190.
66 K. Szymczyk, A. Zdziennicka, B. Janczuk and W. Wójcik, *J. Colloid Interface Sci.*, 2006, **293**, 172–180.
67 N. Kumar, S. Garoff and R. D. Tilton, *Langmuir*, 2004, **20**, 4446–4451.
68 J. H. Snoeijer and B. Andreotti, *Annu. Rev. Fluid Mech.*, 2013, **45**, 269–292.
69 T. S. Chan, T. Gueudre and J. H. Snoeijer, *Phys. Fluids*, 2011, **23**, 112103.
70 T. F. Svitova, M. J. Wetherbee and C. J. Radke, *J. Colloid Interface Sci.*, 2003, **261**, 170–179.